



Green Fenton-like magnetic nanocatalysts: Synthesis, characterization and catalytic application



C. Nadejde^a, M. Neamtu^{a,*}, V.-D. Hodoroaba^b, R.J. Schneider^b, A. Paul^b, G. Ababei^c, U. Panne^{b,d}

^a Interdisciplinary Research Department – Field Science, 'Alexandru Ioan Cuza' University, Lascăr Catargi Str. 54, 700107 Iasi, Romania

^b BAM Federal Institute for Materials Research and Testing, Unter den Eichen 87, 12205 Berlin, Germany

^c National Institute of Research and Development for Technical Physics, Dimitrie Mangeron Bd. 47, 700050 Iasi, Romania

^d Humboldt-Universität zu Berlin, Department of Chemistry, Brook-Taylor-Str. 2, 12489 Berlin, Germany

ARTICLE INFO

Article history:

Received 28 February 2015

Received in revised form 21 April 2015

Accepted 24 April 2015

Available online 25 April 2015

Keywords:

Magnetic core–shell nanocatalysts

Characterization

Fenton oxidation

Micropollutants

Water treatment

ABSTRACT

Five iron oxalate core–shell magnetite nanoparticles catalysts are evaluated as magnetic heterogeneous materials. Simple and efficient procedures for the preparation of magnetic iron oxalate coated nanoparticles are presented. The catalysts are fully characterized using various investigation techniques. Additionally, the formation of photo-sensitized oxygen by spin-trapping using electron spin resonance is investigated. The catalytic activity of two model substrates (carbamazepine and bisphenol A) is also evaluated. The effect of operational parameters (catalyst and H_2O_2 concentration, UVA light) on the degradation performance of the oxidation process is investigated. The obtained reaction rates depend on the nature of the compound and increase with iron oxide shell thickness of the catalyst. Moreover, these materials show a significant activity during two consecutive tests. The optimum experimental parameters are found to be 1.0 g L^{-1} of catalysts, $10\text{ mM }H_2O_2$, under UVA irradiation. More than 99% of both substrates are removed after 30 min of reaction time under the experimental conditions given above. The results obtained show that the catalysts are suitable candidates for the removal of pollutants in wastewaters by means of the Fenton heterogeneous reaction.

© 2015 Elsevier B.V. All rights reserved.

1. Introduction

A wide variety of chemicals, that are not easily biodegradable, are known to bio-accumulate in water organisms, especially in their fatty tissues, and therefore produce serious detrimental reproductive effects on wildlife and humans [1]. Bisphenol A (BPA) is widely used as a raw material for polycarbonate and epoxy resins and is known to accumulate in nature without decomposition. BPA causes reproductive damage to a variety of animal species and has been found to be weakly estrogenic [2]. Carbamazepine (CBZ), an anticonvulsant and mood-stabilizer, has been reported as an anthropogenic marker of urban pollution [3]. One of the most important concerns about the presence of CBZ in the aquatic environment is its potential for bioaccumulation in aquatic biota. The removal of both micropollutants by conventional biological, physical and chemical methods is difficult and costly. The emerging methods for treating water that contains biorefractory organic

pollutants are advanced oxidation processes (AOP), which imply generation and subsequent reaction of hydroxyl radicals, the most powerful oxidizing species after fluorine [4]. However, the high consumption of expensive oxidants, the generated sludge and high operating costs limit the application of the AOPs. Fenton-like processes have been used as a powerful source of hydroxyl radicals from H_2O_2 in the presence of a homogeneous or a heterogeneous catalyst based on a transitional metal cation, under mild reaction conditions and possibly a source of light. Although the homogeneous systems offer a cost-effective source of hydroxyl radicals, there are two major drawbacks that limit the industrial application of this technology: (i) the tight range of pH in which the reaction proceeds and (ii) the need for recovering the precipitated catalyst after the treatment. The resulting sludge may contain organic substances as well as heavy metals and has to be treated further, thus increasing the overall costs. With respect to the weaknesses that the above methods are confronted with, heterogeneous catalytic and photocatalytical processes for wastewater treatment do not have these limits, while offering several advantages and potential benefits. They can be performed under milder conditions (temperature and pressure). Another advantage is the possibility to treat a

* Corresponding author. Tel.: +40 232 201 102; fax: +40 232 201 102.

E-mail address: mariana.neamtu@uaic.ro (M. Neamtu).

single or a group of similar pollutants selectively [5]. Post- or pre-treatment by photocatalysis is an economically feasible possibility to reduce recalcitrant wastewater compounds and achieve a water quality sufficient for reuse. Such an alternative method could be the application of heterogeneous solid Fenton-like catalysts.

The use of magnetic materials as adsorbents or heterogeneous catalysts in water cleanup has attracted increasing attention [6]. Iron oxide magnetic nanoparticles encapsulated in carbonaceous materials, silica, mesoporous silicas or by combining WO_3 [7], have been tested as catalysts in Fenton-like reactions. These materials can be easily removed from water by the simple use of a magnetic field.

Ferrimagnetic catalysts are also known to activate molecular oxygen in air or water and produce reactive oxygen species (ROSs), including hydrogen peroxide (H_2O_2), superoxide radical ($\cdot\text{O}_2^-$), singlet oxygen ($^1\text{O}_2$) and hydroxyl radical ($\cdot\text{OH}$), which are capable of oxidizing contaminants that cannot be removed [6,8][6b,c,8]. Obviously, the combination of abundant iron and molecular oxygen is highly desirable for pollutant control and environmental remediation in view of economic and environmental issues and, therefore, attracts much attention. Several authors reported that unprotected iron oxide nanoparticles could release Fe^{2+} ions into an aqueous phase, promoting in this way the ROS production through Fenton/Haber–Weiss reactions [8]. However, according to other studies, the surface of iron oxide nanoparticles could also play a role in the catalytic ROS production [6][6b]. The rate of the reaction between O_2 and Fe^{2+} ions absorbed onto a mineral was found to be much higher in solution. Moreover, the enormously high surface-to-volume ratio of magnetite is expected to intensify the role of chemical reactions occurring at the surface [8].

A series of studies revealed some adverse effects of iron oxide nanoparticles both in vivo and in vitro [9]. Some of these adverse effects can be effectively reduced by coating the iron oxide nanoparticles with organic ligands. Uncoated magnetite adsorbs oxygen to form maghemite and/or amorphous iron (III) oxide, losing its susceptibility and catalytic activity with time. In addition, the nanosized particles of maghemite form less stable systems, determining their agglomeration. To prevent agglomeration and iron loss, the surface coating of a particle is essential for having stable colloidal dispersion over a wide pH range. The adsorption layer can also enhance the resistance against oxidation of magnetite into maghemite. In this study, in order to improve the stability of iron nanoparticles against aggregation, iron oxalate was chosen. Iron oxalate could be a good candidate to diminish these disadvantages; it is used as a reducing reagent to provide the reducing atmosphere for the synthesis system as well as a coordination ligand to reduce the concentration of free iron ions in aqueous solution. Analogous to previous reports for citrate [10,11] and iron/iron oxide core–shell nanoparticles [12–13], iron oxalate ions could form a shell around each magnetite particle, raising in this way the energy required for the particles to agglomerate, and, consequently, stabilizing the corresponding colloidal suspension.

However, to our knowledge, no study has been carried out on the degradation of BPA and CBZ by iron oxalate coated magnetite. Here we present the characterization and application of five magnetic heterogeneous Fenton catalysts, synthesized by different

procedures. The specific objective of this paper is to investigate the removal efficiency of BPA and CBZ in the presence of magnetite–iron oxalate core–shell nanoparticle catalysts using heterogeneous Fenton-like oxidation and the effects of several parameters such as catalyst loading, H_2O_2 dosage, UV light and behavior of the mixed micropollutants on the oxidation of selected compounds.

2. Experimental

2.1. Reagents and materials

High purity reagents (Sigma–Aldrich) were used in all experiments as purchased without additional purification. Ultrapure water ($18.2\text{ M}\Omega\text{ cm}^{-1}$), obtained with a Barnstead EASYPure® II Ultrapure Water System, was used throughout all synthesis procedures.

2.2. Synthesis of magnetic catalysts

Five magnetic nanocatalysts, based on a magnetite core and a ferrous oxalate shell, were prepared by varying certain parameters during synthesis in order to test their performance depending on their physico-chemical properties (Table 1).

In a first stage, Fe_3O_4 nanoparticles were synthesized using the wet chemical approach (modified co-precipitation method). During the experimental procedure (performed at room temperature), three solutions of $\text{FeCl}_3 \times 6\text{H}_2\text{O}$ (134 mM), $\text{FeSO}_4 \times 7\text{H}_2\text{O}$ (67 mM) and NaOH (2 M) were prepared in distilled deionized water (DDW). Subsequently, the iron salt solutions (in the stoichiometric ratio of 2:1 of Fe^{3+} and Fe^{2+} salts) were mixed together and allowed to reach equilibrium under constant stirring and heating. Precipitation of the iron precursors was immediately initiated by adding dropwise the alkaline precipitation agent (NaOH solution) until pH was 12, into the homogeneous mixture with simultaneous constant heating (75°C) and vigorous magnetic stirring. The formation of NP was marked by the appearance of an intense black precipitate. The resulted mixture was then allowed to settle and cool down onto a permanent magnet followed by repeated washing with DDW in order to remove residual products; the last washing step was carried out with absolute ethyl alcohol for the final product purification. The resulting magnetic slurry was dried in an oven under vacuum at 50°C .

In the next stage, the magnetic nanocatalysts based on magnetite core surrounded by a ferrous oxalate shell were prepared in a post-synthesis procedure. The nanocatalyst samples were prepared as follows:

During the synthesis protocol, Fe_3O_4 dried powder was resuspended in DDW with constant mechanical stirring and heating up to 75°C ; separately, ferrous oxalate ($\text{FeC}_2\text{O}_4 \times 2\text{H}_2\text{O}$) powder was also dissolved in DDW. For the FF1 catalyst, the Fe_3O_4 suspension was added slowly into the $\text{FeC}_2\text{O}_4 \times 2\text{H}_2\text{O}$ solution (at 75°C) with continuous mechanical stirring for two hours. For the second nanocatalyst (FF2), the ferrous oxalate was added in four steps (0.06 g every 15 min) to the Fe_3O_4 suspension (at 75°C) with continuous mechanical stirring for two hours. Three more samples (FF3–FF5) were prepared in a similar manner as the FF2, by

Table 1
Synthesized catalysts.

Catalysts	$\text{Fe}_3\text{O}_4:\text{FeC}_2\text{O}_4 \times 2\text{H}_2\text{O}$ ratio	Synthesis approach
FF1	1:0.310	Fe_3O_4 suspension added to FeC_2O_4 , slowly in one step
FF2	1:0.120	FeC_2O_4 added slowly in four steps, every 15 min
FF3	1:0.090	FeC_2O_4 added slowly in one step
FF4	1:0.067	FeC_2O_4 added slowly in one step
FF5	1:0.045	FeC_2O_4 added slowly in one step

varying the ratio of the two types of materials (Table 1). Subsequently, all nanocatalysts were rinsed several times with ultrapure water and absolute ethanol (to remove impurities and unbound oxalate), followed by drying in a vacuum at 50 °C.

2.3. Characterization

A high-resolution Zeiss Scanning electron microscope (SEM) of type Supra 40 (Carl Zeiss, Oberkochen, Germany) equipped with a Schottky field emitter was employed to characterize the sample surface morphology down to the nanometer scale. The SEM was equipped with an SDD EDS (energy dispersive X-ray spectrometer with silicon drift detector) spectrometer of type X Flash® 5010, from Bruker (Berlin, Germany). With this EDS system a semi-quantitative analysis of the elemental composition of the samples was carried out.

High-resolution transmission electron microscopy (HRTEM) and selected area electron diffraction (SAED) were obtained on a Zeiss Libra 200 MC TEM/STEM electron microscope operating at 200 kV, equipped with an EDS spectrometer of type X Flash® 5030, from Bruker (Berlin, Germany). The samples for TEM were deposited directly on carbon-copper grids.

X-ray diffraction (XRD) patterns were obtained on a Shimadzu LabX XRD-6000 X-ray diffractometer with Cu K α radiation ($\lambda = 1.54178 \text{ \AA}$). A scan speed of 3.00° min $^{-1}$ was applied to record the pattern in the 2 θ range of 20°–70°.

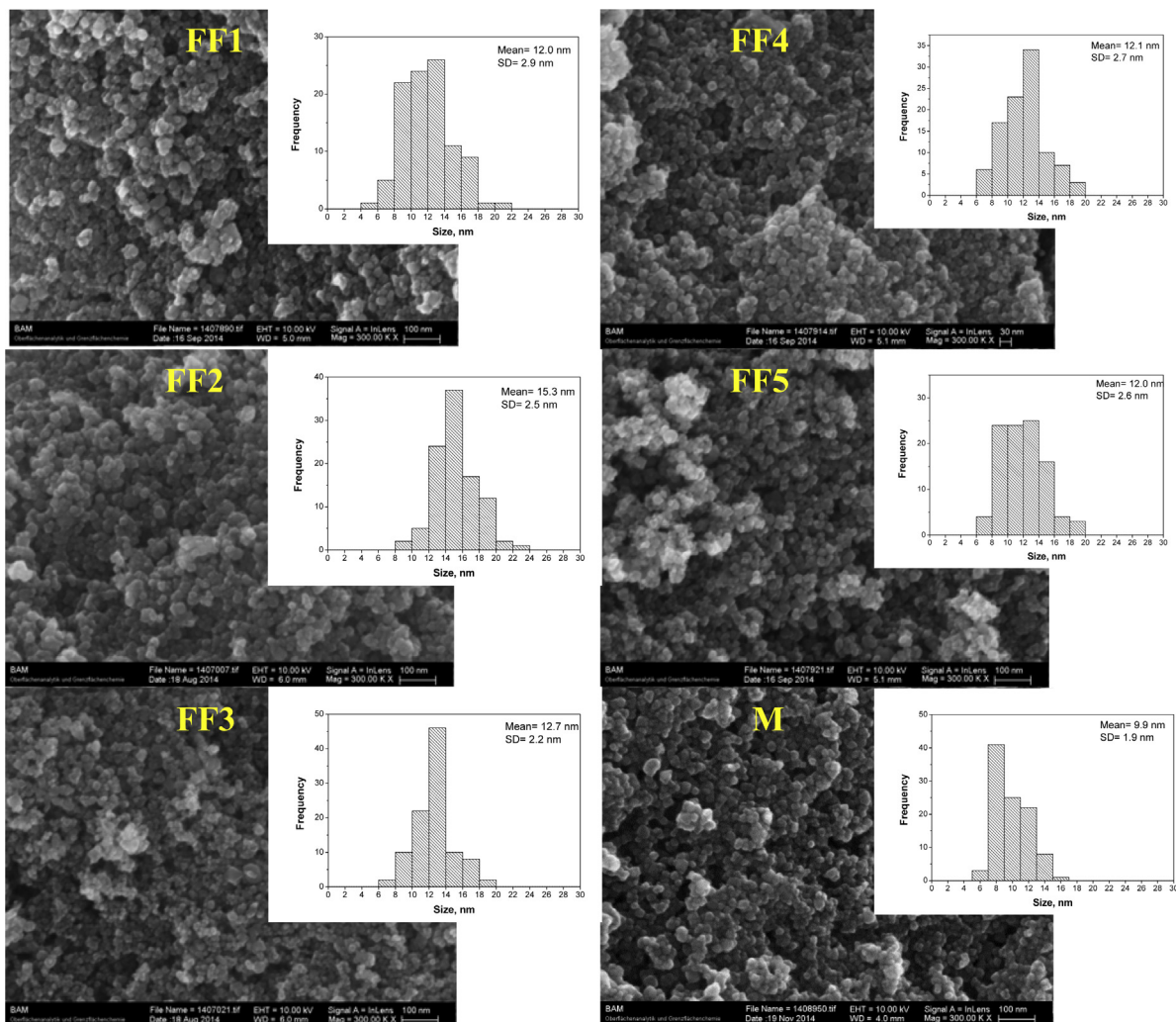


Fig. 1. SEM micrographs and particle size distributions of the nanocatalysts (FF1 to FF5) and uncoated magnetite (M).

Infrared spectra of all samples were measured on a Jasco 660 Plus spectrometer in KBr disk, between 4000 and 400 cm $^{-1}$, with a resolution of 4 cm $^{-1}$.

A Vibrating sample magnetometer (VSM) MicroMag Model 2900/3900 was used on the powdered samples for the measurement of magnetic properties.

The nitrogen adsorption and desorption isotherms, the Brunauer–Emmett–Teller (BET) tests were performed with a Micromeritics ASAP 2020™ Physisorption system (Norcross, USA) at 77 K. Interparticle space distribution was determined by the Barrett–Joyner–Halenda (BJH) method. Before analysis, the samples were degassed for 4 h at 105 °C under vacuum.

2.4. Electron spin resonance (ESR) experiments

Before ESR detection of the photo-sensitized $^1\text{O}_2$, the 5-mL sample volumes of aqueous suspensions containing the catalyst, pollutant and 40 mM of 2,2,6,6-tetramethyl-4-piperidinol (TMP-OH) were transferred into a small dark vial and exposed to UVA ($\lambda = 365 \text{ nm}$ from a UV spot light source Lightingcure™, model LC-8, from Hamamatsu Photonics, Germany. Photon flow of $2.19 \times 10^{-7} \text{ Einstein s}^{-1}$, irradiation depth of 1.4 cm, irradiated surface of 4.90 cm 2). The illumination was performed at the room temperature. During illumination, the suspensions were equilibrated with oxygen at the atmospheric pressure.

To acquire ESR traces, small aliquots of *ca.* 50 microliters of illuminated suspensions were transferred into 0.7 mm ID and 0.87 mm OD glass capillary tubes, with a sample height of *ca.* 40 mm, and sealed on both ends with Cha-seal (Tube sealing compound, Chase Scientific Glass, Rockwood, TN, USA) and then placed into quartz glass tubes with an inner diameter of 4 mm (Magnetech GmbH, Berlin, Germany). Continuous wave X-band ESR-Spectra of TEMPOL formed from TMP-OH were recorded at room temperature using an ESR Spectrometer (MiniScope MS 300, Magnetech GmbH, Berlin, Germany) at a microwave power of 0.1 mW. An internal manganese standard (Mn^{2+} in ZnS) was measured simultaneously with the samples. The typical instrumental settings were: B0-field 336 mT, sweep width 10 mT, sweep time = 60 s, and a modulation amplitude of 0.2 mT.

2.5. Kinetic experiments

Solutions containing the micropollutants were prepared by adding an appropriate volume of stock solution to ultrapure water for the final concentration. The oxidation experiments, in absence of UVA light, were carried out on a rotator SB3 (VWR International, Germany), whereas in the presence of UVA irradiation the experiments were conducted using an orbital shaker Heidolph Titramax 100 with continuous mixing. The initial pH of the micropollutant solution was 6.6 without any adjusting. After stabilization, the solution was analyzed to confirm the absence of adsorption by the catalysts. No noticeable removal of pollutants by adsorption on catalyst was obtained during heterogeneous Fenton-like oxidation experiments for all the catalysts synthesized. Then a solution of 30% H_2O_2 was added to achieve the selected H_2O_2 concentrations (10 and 20 mM), these being the basic conditions for the experiments. Samples of the reaction medium were withdrawn at regular intervals and filtered immediately through a 0.22 μm Teflon membrane filter for HPLC analysis.

All photochemical experiments were performed using three parallel ordered UVA nm xenon lamps (ATLAS Material Testing Solution, Germany). The UV intensity was 40 W m^{-2} . The photon flow in the UV range ($290 \leq \lambda \leq 400\text{ nm}$) of the solar UV simulator measured by polychromatic actinometry with phenylglyoxylic acid in $AcN:H_2O = 3:1$ (v/v) [14] was 2.13×10^{-7} Einstein s^{-1} . The total reaction volume was 8 mL in all experiments; the diameter of the irradiated surface area was 9.62 cm^2 and the irradiation path-length 1.4 cm. The relative standard deviation of three experiments was less than 4%.

2.6. Analyses of micropollutants

Sample analysis was performed by HPLC-MS/MS. A series 1100HPLC workstation (Agilent Technologies, Waldbronn, Germany) was coupled to an API 4500 TSQ triple stage quadrupole mass spectrometer (ABSciex, Darmstadt, Germany) (see SI).

3. Results and discussion

3.1. Characterization of the catalysts

The morphology of the sample surface and the size of the primary particles were examined by high-resolution SEM and TEM. The effect of varying the oxalate concentration used for the synthesis of the catalysts on the morphology at the nanometer scale was also investigated. The SEM images show that the samples are agglomerated with agglomerates sizes over a large range of several μm up to more than 100 μm . The individual nanoparticles of rather spherical-like shape have a size between 10 and 20 nm. Thus, the primary nanoparticles confer a coarse sample surface at the nanoscale. The addition of oxalate does not alter the morphology of the initial iron oxide samples as shown by the high-resolution micrographs of the coated catalysts (FF1 to FF5) and of the uncoated magnetite (M) in Fig. 1.

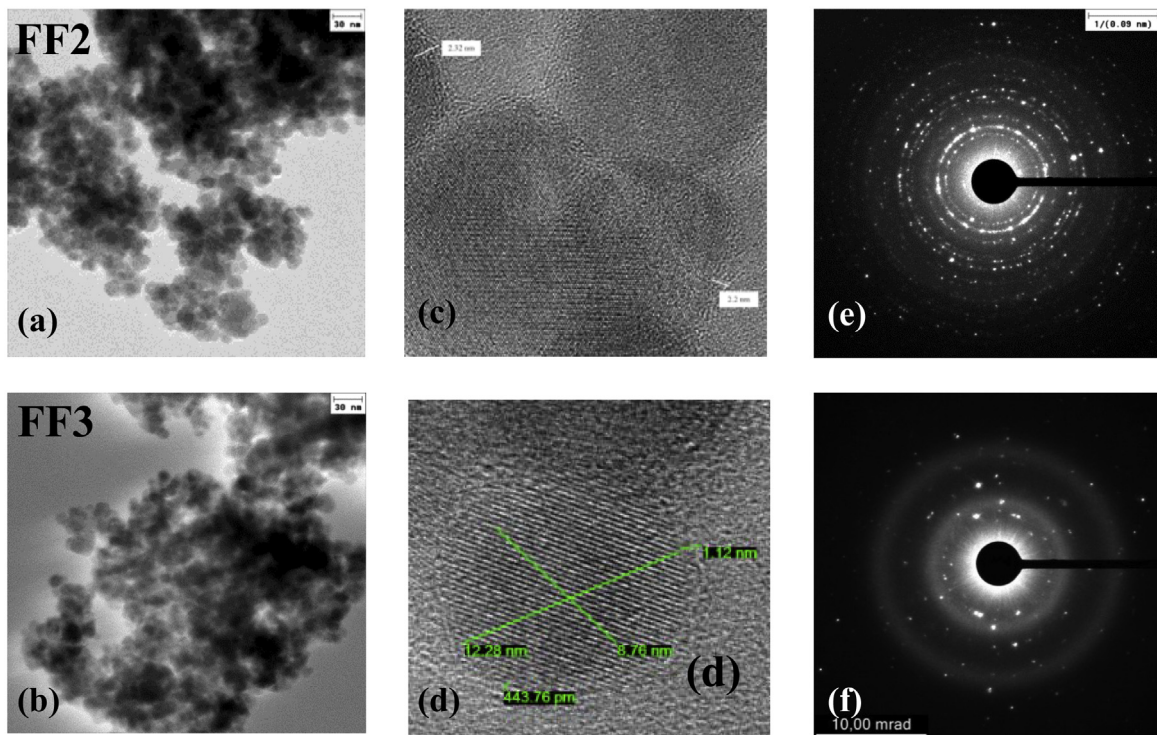


Fig. 2. TEM images of FF2 (a) and FF3 (b) at low (left) and at a high magnification (middle) together with corresponding SAED patterns (right) taken from sample areas of about 180 nm diameter. The high magnification images show examples of the size of selected cores and the thickness of selected shells.

The high-resolution images as taken with SEM have been processed so that a rough size distribution of the primary particles can be extracted from each image for comparison purposes. The size of one hundred primary particles in each SEM image in Fig. 1 has been measured “by hand” by means of the image processing software ImageJ (Rasband WS (1997–2009)) and the obtained particle size distributions (PSD) show a mean value of 12 nm for the images corresponding to the samples FF1, FF4 and FF5. From the FF3 image a slightly higher mean value of 13 nm can be derived, and from the FF2 image a significantly larger PSD mean value of 15 nm could be determined. The standard deviation of the obtained PSD is about 2–3 nm. As expected, the analysis of the SEM images of the original magnetite provides PSDs with lower mean values of about 10–12 nm. Note that these PSDs should be considered as a rough estimation of the mean size of the primary particles constituting the samples; nevertheless, there was a tendency for the more catalytically active samples to display also a somewhat larger mean size of the primary nanoparticles. Moreover, the mean size of the primary particles as measured by SEM is in agreement with the sizes of the selected particles as observed in TEM (see below). It should be noted that primary particles of 10 nm size might well be core–shell structures – as reported in the literature – however, even a high-resolution SEM cannot resolve such structures in the nanometer range.

In order to clarify the role of oxalate in the possible formation of a spherical nano-product, HRTEM was carried out, see Fig. 2(a)–(f), which confirmed the core–shell structures of the catalysts. TEM measurements show the presence of roughly the same ultrathin shell of 1–2 nm. Furthermore, the cores are constituted of crystalline material and the shells are amorphous in nature. The amorphous structure of the shells is visible in the TEM images rather than in the SAED patterns. In the Fig. 2(e) the SAED ring corresponding to the amorphous shells is “covered” by the small-spots rings corresponding to the Fe_3O_4 nanocrystalline structures. In Fig. 2(f) the SAED ring corresponding to the amorphous shells is more visible relative to that one from Fig. 2(e). Both findings are consistent with results reported earlier for core–shell iron oxide nanoparticles [10,6][10,6b]. Fig. 2(e) and (f) also show the corresponding SAED patterns taken from an about 180 nm diameter area of samples FF2 and FF3 prepared onto TEM grids. The diffraction rings confirm that the magnetite cores are polycrystalline. From inside to outside of the SAED pattern the rings can be indexed to the (1 1 1), (2 2 0), (3 3 1), (4 0 0), (5 1 1), (4 4 0) planes of spinel Fe_3O_4 , respectively.

Energy dispersive X-ray spectroscopy (EDX) was applied to gain information on the elemental composition of the samples from selected “bulk” (more tens of μm size) agglomerates, see Fig. 3.

As expected, the EDX spectra show only Fe, O and C as main elements present in the samples. At first sight the spectra are nearly similar. In order to be able to differentiate between possible small variations in the Fe and O relative content, the spectra were normalized to the intensity of the O K peak at 525 eV. The advantage of this kind of semi-quantitative analysis is that differences in the Fe concentration can be directly read from the intensity of the Fe L α peak at 705 eV even when the morphology of the sample surfaces is quite rough. Note that the direct comparison of the Fe/O concentration ratio is physically justified by the similar behavior of the two characteristic X-ray lines in the sample: the two lines of close low energies are susceptible to significant self-absorption, however, similarly absorbed. For each sample 2–3 locations were measured and the EDX spectra were summed up to get better statistics. The final result is that the Fe/O ratio is higher for FF3 and FF2 than for FF5, FF1 and FF4. In order to validate the small differences extracted from the EDX spectra at 20 kV, another series of EDX measurements at 5 kV acceleration voltage was carried out. This more surface sensitive result confirms in great measure the findings described above for 20 kV. Only FF5 provides a higher Fe/O intensity ratio – similar to that of FF3. Furthermore, the main variations of the Fe/O concentration ratios as found by EDX at SEM were confirmed in general by the EDX results on electron-transparent samples prepared for TEM.

It should be noted that the SEM/EDX measurements were performed at another time than the TEM/EDX measurements and the sample surface might have slightly changed with respect to surface contamination. As far as the variation of carbon is concerned, this is a challenging issue due to the unavoidable presence of contamination at the surface of the porous samples – a typical artifact observable in electron microscopy. Nevertheless, the significantly higher intensity of carbon for the FF2 sample is noticeable.

FTIR analysis was employed to study the binding of iron oxalate on magnetite surface. Fig. 4(a) depicts the IR spectra of the uncoated and coated magnetite nanoparticles and of iron oxalate. The IR bands at low wave numbers ($\leq 700 \text{ cm}^{-1}$) correspond to the vibrations of Fe–O bonds of iron oxide [15]. The free C=O stretching peak typically occurs at $\sim 1700 \text{ cm}^{-1}$, however upon complexation with Fe_3O_4 the C=O_{oxalate} bond is weakened and the IR band shifts to the right. The observed peak at $1680\text{--}1687 \text{ cm}^{-1}$ is assigned to C=O_{oxalate} and is an indicative of complexation of the iron oxalate by the magnetite surface. This signal is more pronounced in the case of FF2 and FF3 catalysts.

The XRD patterns of the uncoated and coated iron oxide particles prepared with different concentrations of iron oxalate were presented in Fig. 4(b). The 2θ values of the peaks are compared with the standard data for uncoated Fe_3O_4 . It is found that the intensities and d values of the peaks in the obtained XRD pattern match well

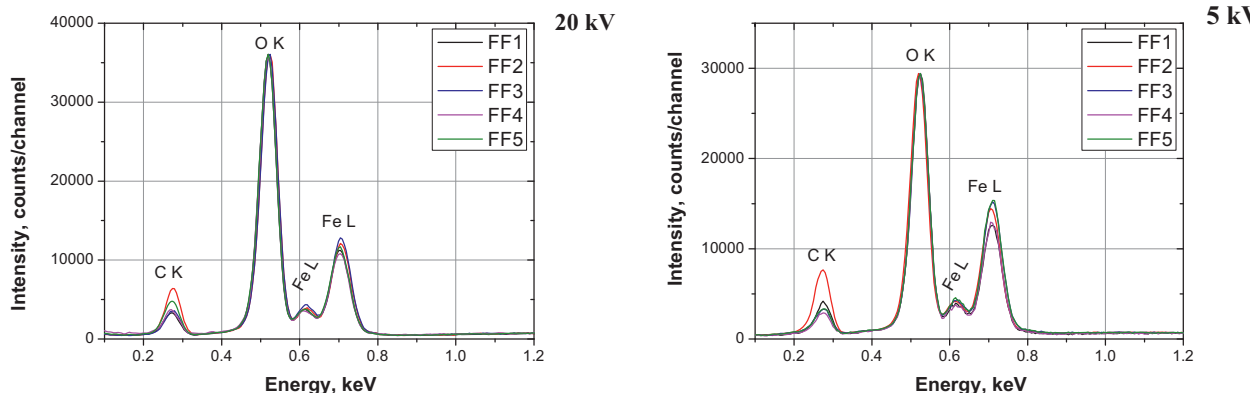


Fig. 3. EDX spectra of the five samples (FF1 to FF5) at 20 and 5 kV normalized to the O K peak intensity.

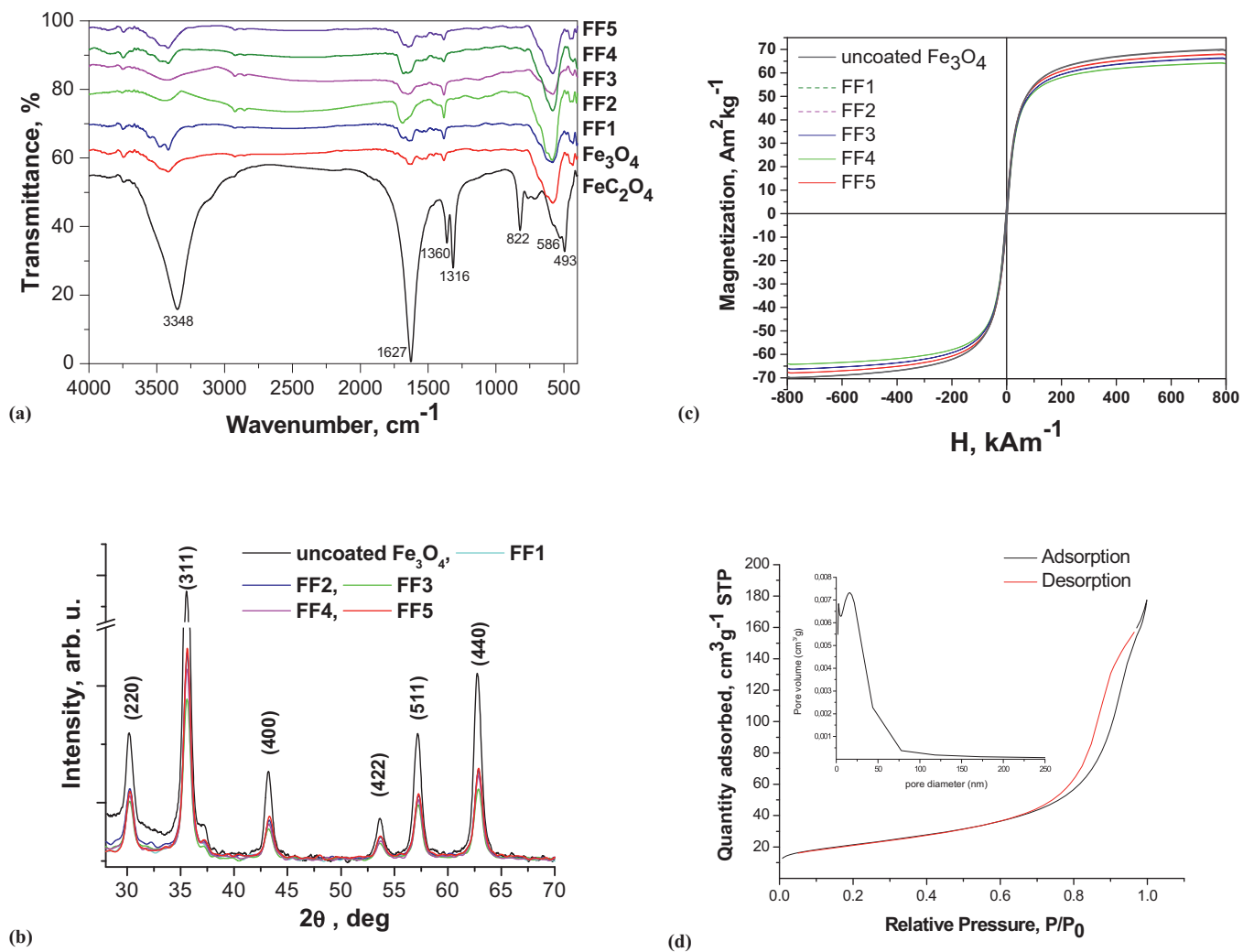


Fig. 4. FTIR spectra (a), X-ray diffractograms (b), room temperature hysteresis curves (c) of synthesized catalysts (FF1 to FF5) and uncoated magnetite, and the nitrogen adsorption–desorption isotherm and pore size distribution curve (inset) (d) of FF2 catalyst.

with the Fe_3O_4 phase (JCPDS Card No. 75-033). In addition, in our XRD pattern there are no typical $\gamma\text{-Fe}_2\text{O}_3$ (JCPDS card No. 39-1346) peaks such as (110), (210), (211), so that the absence of $\gamma\text{-Fe}_2\text{O}_3$ is indicated. The main peaks at 2θ values of 30.20, 35.60, 43.25, 53.66, 57.18 and 62.75° in the diffraction pattern curves in Fig. 4(b) can be indexed to the (220), (311), (400), (422), (511) and (440) faces of magnetite, respectively. The XRD patterns of coated magnetite are typical for pure magnetite, however, a slight decrease in the peak intensities can be observed with the increase of the iron oxalate content in the sample preparation, most significantly for the FF3 catalyst. This can be attributed to the enhanced absorption of X-ray due to Fe cations in the core–shell layer [16].

Fig. 4(c) shows the magnetic hysteresis curves of the coated catalysts and of the uncoated magnetite. The samples are superparamagnetic at room temperature and exhibit typical superparamagnetic behavior with no hysteresis loops. The highest saturation magnetization is displayed by uncoated magnetite ($M_s = 69.36 \text{ Am}^2 \text{ Kg}^{-1}$ at 790 KA m^{-1}), whereas the iron oxalate coated nanoparticles hold a M_s around $65.53 \text{ Am}^2 \text{ Kg}^{-1}$ at 790 KA m^{-1} , i.e., $66.98 \text{ Am}^2 \text{ Kg}^{-1}$ for FF1, $63.43 \text{ Am}^2 \text{ Kg}^{-1}$ for FF2, $65.85 \text{ Am}^2 \text{ Kg}^{-1}$ for FF3, $63.85 \text{ Am}^2 \text{ Kg}^{-1}$ for FF4, and $67.53 \text{ Am}^2 \text{ Kg}^{-1}$ for FF5, that is consistent with the results reported for particles with similar sizes [17].

The nitrogen adsorption isotherm of the FF2 catalyst is shown in Fig. 4(d). The obtained N_2 adsorption isotherms for the samples

are of type IV according to IUPAC, with curves showing an apparent hysteresis at a relative pressure of P/P_0 between 0.7 and 1.00. This demonstrates that the catalysts can be considered as mesoporous materials. The plot of pore size distribution determined by the BJH method shows that there are two peaks in the mesoporous range (2–50 nm), a dominant peak around 16.4 nm and a small peak at 2.6 nm. The mesopores on spheres can be attributed to the interspaces of constituent particles. The BET specific surface area of sensitized nanomaterials is around $80 \text{ m}^2 \text{ g}^{-1}$, i.e., $69.46 \text{ m}^2 \text{ g}^{-1}$ for FF1, $77.03 \text{ m}^2 \text{ g}^{-1}$ for FF2, $78.75 \text{ m}^2 \text{ g}^{-1}$ for FF3, $82.81 \text{ m}^2 \text{ g}^{-1}$ for FF4, and $78.26 \text{ m}^2 \text{ g}^{-1}$ for FF5, which is nearly 12 times and 6 times larger than that of commercial magnetite (BET surface area of $6.2 \text{ m}^2 \text{ g}^{-1}$) and of that reported in the literature ($13.5 \text{ m}^2 \text{ g}^{-1}$), respectively [18]. The measured BET surface areas are in good agreement with the expected/theoretical values of $77\text{--}96 \text{ m}^2/\text{g}$ in the assumption that the primary particles are spherical, contain no internal porosity, have a mean diameter of 12–15 nm (according to the SEM derived PSDs) and have a density (of magnetite) of 5.2 g cm^{-3} . The pore volume and pore diameter of FF2 (for example) are around $0.274 \text{ cm}^3 \text{ g}^{-1}$ and 14 nm, respectively. The results are similar with those reported for citrate core–shell magnetite [10].

To follow the formation and quenching of the photosensitized singlet molecular oxygen, ${}^1\text{O}_2$, generated by the FF2 catalyst, the ESR was employed by using 2,2,6,6-tetramethyl-4-piperidinol (TMP-OH) as spin traps. According to the literature, the diamagnetic

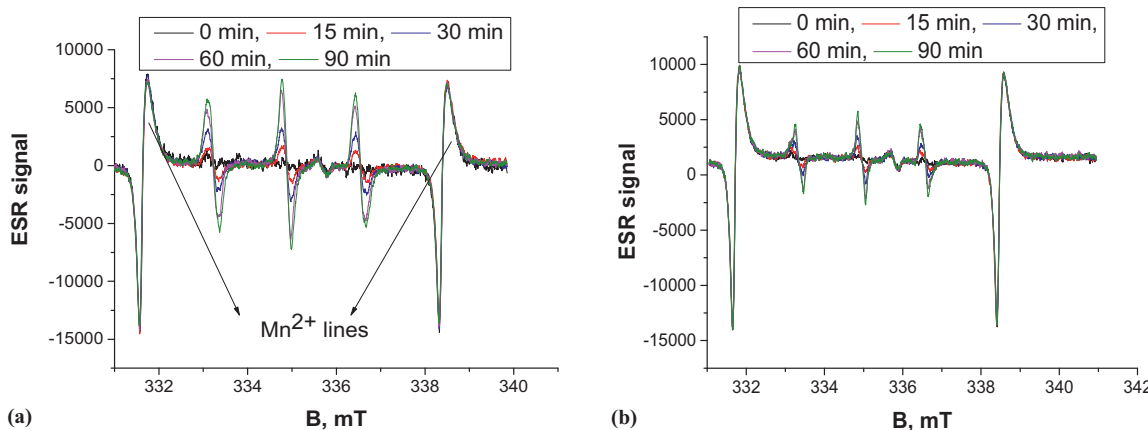


Fig. 5. The ESR spectra of TEMPOL acquired during 90 min of UV illumination ($\lambda = 365$ nm) of TMP-OH solution in the presence of the FF2 catalyst (a) and of control solution (b). Initial conditions: 1 g/L FF2 catalyst, 40 mM of TMP-OH, photon flow of 2.19×10^{-7} Einstein s $^{-1}$, irradiation depth of 1.4 cm, irradiated surface of 4.90 cm 2 , room temperature. The intensity of the manganese line in Figure arises from the internal manganese standard (Mn^{2+} in ZnS) measured simultaneously with the samples.

Table 2
Concentration of $^1\text{O}_2$ (μM) generated in different ESR experiments.

Time, min	FF2 + TMP – OH + UV	TMP – OH + UV	CBZ + TMP – OH + UV	Rose Bengal + TMP – OH + UV
0	0	0	0	0
5	0.23	0.16	0.10	3.93
10	0.41	0.25	0.16	11.45
15	0.52	0.38	0.23	17.40
30	0.95	0.62	0.54	27.03
45	1.41	0.78	0.82	31.57
60	1.87	0.97	1.11	n.d.
90	3.75	1.20	1.19	n.d.

scavenger TMP-OH reacts with $^1\text{O}_2$, yielding a stable paramagnetic product, 4-hydroxy-2,2,6,6-tetramethylpiperidine-1-oxyl (TEMPOL) [19] that can be easily detected by ESR. Although other ROS can also lead to formation of TEMPOL [20], the reactive scavenging of $^1\text{O}_2$ by TMP-OH is considered to be highly specific for $^1\text{O}_2$ [21]. Fig. 5 shows the ESR spectra obtained from the samples containing TMP-OH in the presence of catalyst (a) and in its absence (b), under UVA illumination.

Three equidistant and equi-intense hyperfine lines in ESR spectrum, with spectral parameters $\Delta H_{\text{pp}} = 1.58$ G, $g = 2.00570$, and $a_N = 17.13$ G, are typical for TEMPOL, which was proven by using a TEMPOL reference (not shown). As Fig. 5(b) shows, a low marked ESR signal could be observed for the samples containing only TMP-OH exposed to UV illumination for 90 min. In contrast, after a 90-min exposure to UV light, the solution containing the catalyst, as well as the control solution (containing only TMP-OH), showed a characteristic ESR signal (Fig. 5(a)). The signal intensity of the TEMPOL spectra acquired for the catalyst is larger than for the control solution.

This might suggest that, under exposure to UV light, the catalyst contributed to the overall singlet oxygen formation. The ESR experiments point to an efficient formation of $^1\text{O}_2$ by the studied catalyst in aqueous suspension. Using Rose Bengal as a reference sensitizer, the corresponding singlet oxygen concentrations could be calculated. In the presence of the catalyst (3.75 μM) about 3 times more $^1\text{O}_2$ was generated than in its absence (1.2 μM , Table 2).

According to Ai et al. [6][6b] more surface bound ferrous ions could form with an increase of iron oxide shell thickness and then promote the single-electron molecular oxygen activation pathway to generate more ROS. Some researchers have also reported the generation of superoxide and hydroxyl radicals in Fe based nanoparticle systems [8,6][8,6b]. The experiments conducted by Voinov et al. [8] with 0.24 mM FeCl_3 or $\text{Fe}(\text{NO}_3)_3$, simulating the iron ions leached from the nanoparticles, confirmed that the

observed catalytic activity of the $\gamma\text{-Fe}_2\text{O}_3$ and Fe_3O_4 nanoparticles is attributed primarily to the reactions at the nanoparticles' surface, rather than being caused by the dissolved metal ions released by the nanoparticles as previously thought.

In our experiments the leached iron content was between 50 and 230 $\mu\text{g L}^{-1}$ in absence and in presence of hydrogen peroxide, respectively, after 2 h of UVA light exposure, with much lower concentrations than the ones used by Voinov et al. [8], and well below the limit set by the EU directives ($<2.0\text{ mg dm}^{-3}$). In these conditions, the amount of pollutant degraded by homogeneous catalysis resulting from leached iron is probably negligible.

3.2. Catalytic and photocatalytic activity

In order to find out the optimal conditions for catalytical and photocatalytical performance of the catalysts, a series of comparative degradation experiments on pollutants were performed. The studies were carried out at the pollutants' initial concentration of 0.5 μM at room temperature. The effects of the concentration of the catalyst, H_2O_2 and UVA light were investigated. The (photo)-degradation of CBZ and BPA was carried out after adsorption/desorption equilibrium had been reached between pollutants and the catalysts. The influence of catalyst concentration on pollutant removal was studied, from the practical point of view, at nearly neutral pH (6.6), by using solutions with pH values determined initially and without any modifications or control of the pH during the process.

In Fig. 6(a) the results obtained for CBZ and BPA removal as a function of the initial concentration of the five catalysts in absence of UVA light at various reaction times are presented. The degradation of CBZ was faster than for BPA (Fig. 6).

The maximum conversion of over 66% was achieved after 120 min from the start of the reaction for CBZ over FF2. After 30 min of catalytic oxidation with a dose of 1.0 g L^{-1} FF2 the removal was

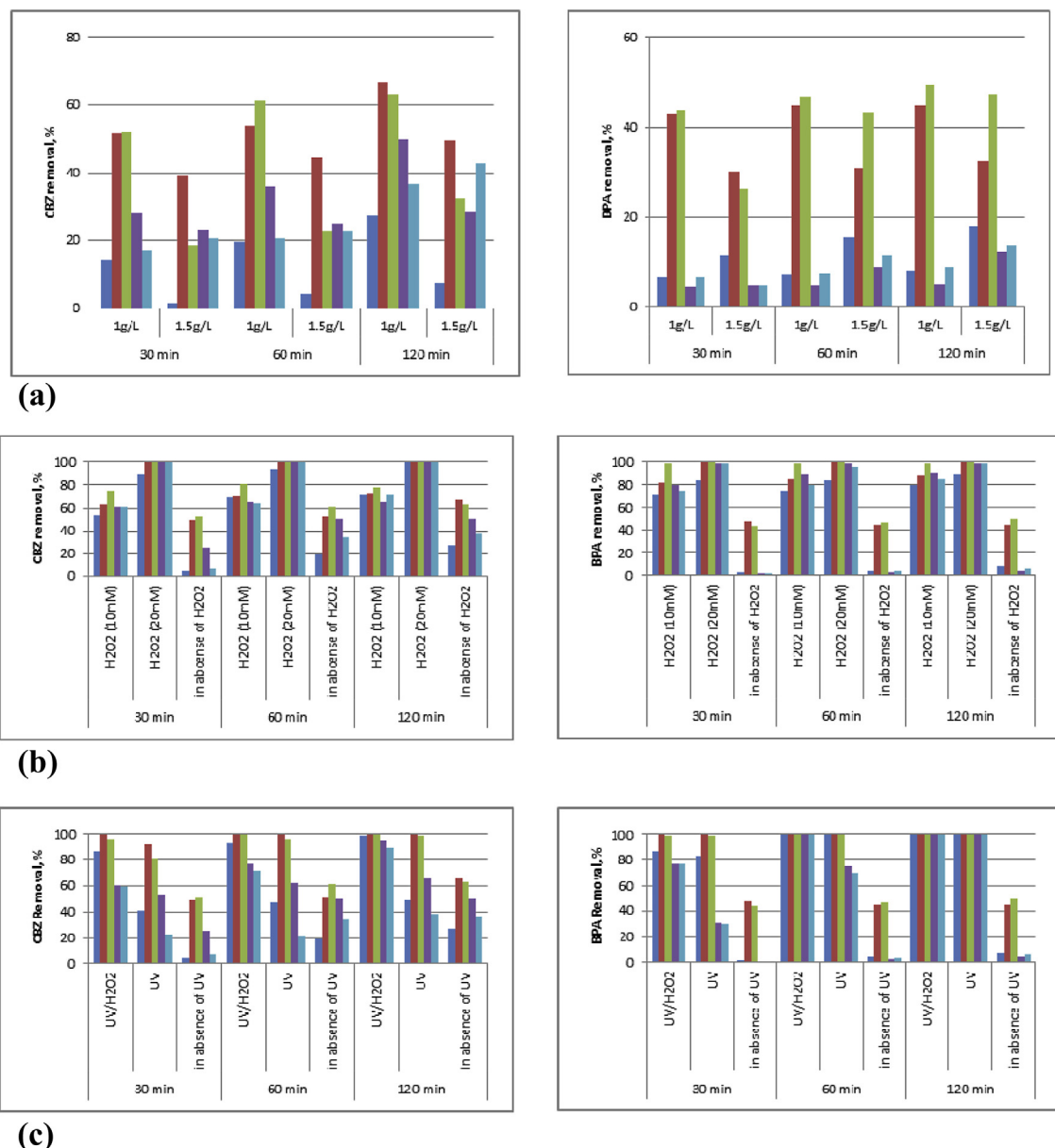


Fig. 6. The effect of catalyst dosage (a), H_2O_2 concentration (b) and UV light (c) on pollutants removal. Initial conditions: $0.5 \mu\text{M}$ of the pollutant, pH 6.6, 25°C , 1.0 g L^{-1} catalyst (b, c), 10 mM H_2O_2 (c). FF1 – dark blue, FF2 – red, FF3 – green, FF4 – purple, FF5 – blue. (For interpretation of the references to color in this figure legend, the reader is referred to the web version of this article.)

around 50%. More than 66% of CBZ and 45% of BPA were removed over 1.0 g L^{-1} of FF2 and FF3 in absence of H_2O_2 in 2 h. Significantly lower efficiencies of 4.4%, 6.1% and 7.8% for FF4, FF5 and FF1 were observed for BPA degradation. However, by further increasing the amount of catalyst to 1.5 g L^{-1} , no increase in removal was observed for both pollutants. This observation leads to the suggestion that an optimum concentration for the catalyst could be 1.0 g L^{-1} . Thus, we selected the concentration of 1.0 g L^{-1} of catalyst for our further experiments. The above results clearly demonstrated that both pollutants could be oxidatively degraded with dissolved oxygen in water over the catalysts, involving a molecular oxygen activation process. Since the dissolved oxygen and the initial pH were the same during all the degradation experiments, the different aerobic degradation efficiencies of pollutants might be ascribed to the reactivity of the catalysts. As is known, the surface area could affect the reactivity of catalysts. The BET specific surface area of the catalysts is roughly the same (from $69 \text{ m}^2 \text{ g}^{-1}$ for FF2 to $83 \text{ m}^2 \text{ g}^{-1}$ for

FF3, suggesting that the different reactivity of the catalysts is not attributed to the surface area, but to the iron oxalate shell surrounding the magnetite primary NPs caused by higher concentration of iron oxalate. Similarly, Ai et al. [6][6b] reported that the best catalytical efficiency is provided by the core–shell $\text{Fe}@\text{Fe}_2\text{O}_3$ catalyst with higher shell thickness.

As proposed in the literature, we can assume that the ferrous ions, bound on the surface of iron oxide, could activate molecular oxygen via a single-electron reduction pathway producing ROS that are capable of reducing the pollutants [8,22]. Our results on singlet oxygen formation support this assumption. We also found that the degradation of CBZ was negligible in the presence of pure magnetite, revealing that the higher reactivity of the catalysts was not attributed to the magnetite, but to the surface bound ferrous oxalate. As known, h_{VB}^+ and e_{CB}^- occupy important positions in the degradation of organic molecules because they are responsible for the production of oxygen reactive species [23]. The cause

for the low removal at higher catalyst concentration could probably be the overlapping agglomerates. Consequently, the electron transfer from the iron core to the iron oxide shell and subsequent electron transportation within the iron oxide shell would become slower and could even be gradually blocked. Thus, the two-electron reduction molecular oxygen activation for the generation of ROS would be inhibited [6b,24].

The presence of iron ions in the solution could promote additional generation of ROS by homogeneous Fenton reaction. It is noticeable that the catalyst leaching in our experiments remains low (between 50 and 230 $\mu\text{g L}^{-1}$ after 2 h of reaction at 1.0 g L^{-1} catalyst in the absence and presence of 20 mM H_2O_2 , respectively). Under these conditions, the amount of pollutant degraded by homogeneous catalysis resulting from leached iron is negligible. Similar results were reported by Centi et al. [25] and Ai et al. [6][6b] for the catalytic wet peroxide oxidation of carboxylic acids and 4-chlorophenol, respectively.

In the next step, the kinetic studies of catalytic oxidation with different hydrogen peroxide concentrations were carried out using the same operational conditions: $\text{pH} = 6.6$, $t = 25^\circ\text{C}$ and 1.0 g L^{-1} of catalyst. The results are presented in Fig. 6(b). As expected, increasing hydrogen peroxide concentrations accelerated the removal of pollutants. This can be explained by the effect of the OH^\bullet radicals produced additionally. After 30 min of reaction time at a dose of 10 mM H_2O_2 , 75% of CBZ and 98% of BPA removal were achieved, whereas after 60 min of the reaction both pollutants were completely removed. A further increase in the H_2O_2 concentration did not significantly influence the conversion of the pollutants. Effective system conditions for further experiments were found to be $\text{pH} = 6.6$, $t = 25^\circ\text{C}$, catalyst concentration of 1.0 g L^{-1} and 10 mM H_2O_2 . The best catalytical activity was provided by FF2 and FF3 catalysts. A previous study [26] has reported that over 1.0 g L^{-1} of uncoated Fe_3O_4 in the presence of 100 mM H_2O_2 only 6% of CBZ was degraded after 120 min of reaction, whereas at the same condition in the presence of 0.5 mM of nitriloacetic acid more than 99% of CBZ was removed. Our results clearly show that coating of magnetite with ultrathin iron oxalate enhances the degradation efficiency of pollutants.

Micropollutant degradation was also investigated using simulated solar light (UVA) in the presence and absence of hydrogen peroxide. Fig. 6(c) shows the removal of micropollutants versus irradiation time at different hydrogen peroxide doses. A small conversion of pollutants was observed, when exposed to UVA light in the absence of H_2O_2 . In the presence of H_2O_2 and UVA light, the conversion substantially increased due to the hydroxyl radicals generated during the photochemical reactions. After 30 min of irradiation in absence of H_2O_2 the removal rate of CBZ in ultrapure water was only 23% for FF5 and 92% for FF2, whereas the BPA removal was higher than 30% for FF5 and BPA was completely removed in the presence of FF2. At the same reaction time, by adding 10 mM H_2O_2 , more than 96.6% and 99.9% of CBZ and almost completely of BPA were removed in the presence of FF3 and FF2, respectively. After 60 min of irradiation, around 71% of CBZ was degraded in the presence of all catalysts.

Obviously, pharmaceuticals do not occur in the environment as single contaminants, but rather as a complex mixture of a whole variety of pharmaceuticals and contaminants. It has been suggested that the overall environmental toxicity of a complex mixture of pollutants can be much larger than the toxic effect of individual chemical agents [27]. Therefore, the degradation of both micropollutants has been also investigated simultaneously in the mixture, at the same molar concentration (Fig. 7).

The removal rate was lower than that in the experiments with individual compounds. This could be probably explained by the competition of micropollutants for reactive oxygen radicals. The presence of 10 mM of H_2O_2 and UV irradiation provided the

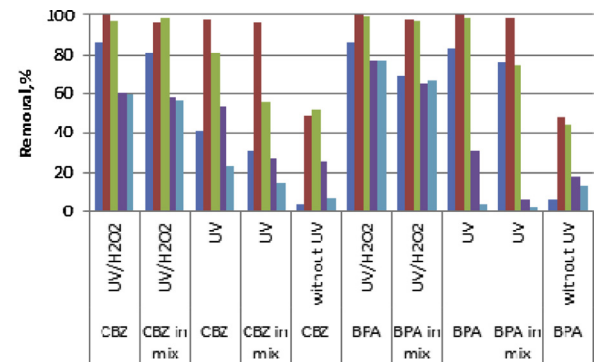


Fig. 7. The degradation of the pollutants in the mixture. Initial conditions: 0.5 μM of the pollutant, pH 6.6, 25 $^\circ\text{C}$, 1.0 g L^{-1} catalyst, 10 mM H_2O_2 , reaction time 30 min. FF1 – dark blue, FF2 – red, FF3 – green, FF4 – purple, FF5 – blue. (For interpretation of the references to color in this figure legend, the reader is referred to the web version of this article.)

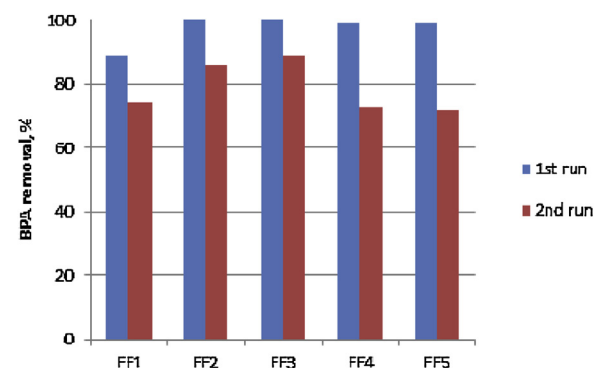


Fig. 8. Stability and reusability experiments. Initial conditions: 0.5 μM of the pollutant, pH 6.6, 25 $^\circ\text{C}$, 10 mM H_2O_2 , reaction time 2 h.

highest removal of micropollutants. 97% of both micropollutants have been degraded in the first 30 min over FF2 and FF3 in the presence of H_2O_2 . After the same reaction time, in absence of H_2O_2 , the removal rate of CBZ was lower over FF3 (56%), whereas the BPA removal rate was 74%. The degradations of CBZ and BPA were lower over FF1, FF4 and FF5. Again, the most active catalysts were obviously FF2 and FF3.

In order to evaluate the applicability of the catalysts in water treatment, the catalytic materials should be (i) easily removed from the effluent, and (ii) reused several times without loss of activity. Therefore, we performed some catalytic experiments while reusing the catalysts. The coated magnetite nanoparticles have been removed from the effluent after 2 h of treatment, during two consecutive catalytic tests, and characterized after these tests. After each run, the solid powder was magnetically separated from the solution, and then rinsed with water to remove any possible contaminant from the surface, and finally dried at 50 $^\circ\text{C}$. The results of the tests are summarized in Fig. 8. It was observed that after two repeated experiments, the catalyst retained a good activity, despite a slight decrease in BPA removal after 2 h from 100% to 86–89%.

Based on the high-resolution SEM images, the morphology of the samples before and after catalytical experiments is very similar at the nanoscale (Fig. 9), corresponding to the FF2 sample.

Moreover, the roughly spherical shape of the primary (nano) particles remains unchanged after treatment. No significant differences could be established between the average size of about 10–20 nm of the constituent particles before and after treatment.

The possible change in the elemental composition after catalytic experiments was also investigated by EDX. Two representative EDX

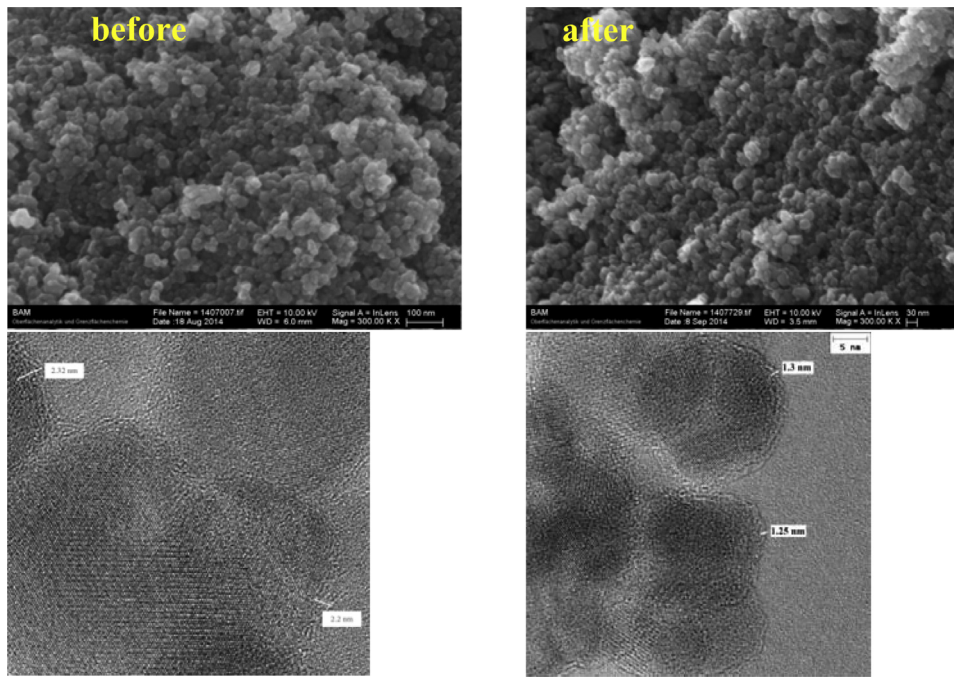


Fig. 9. SEM micrographs and TEM images of FF2 catalyst before and after the catalytical treatment.

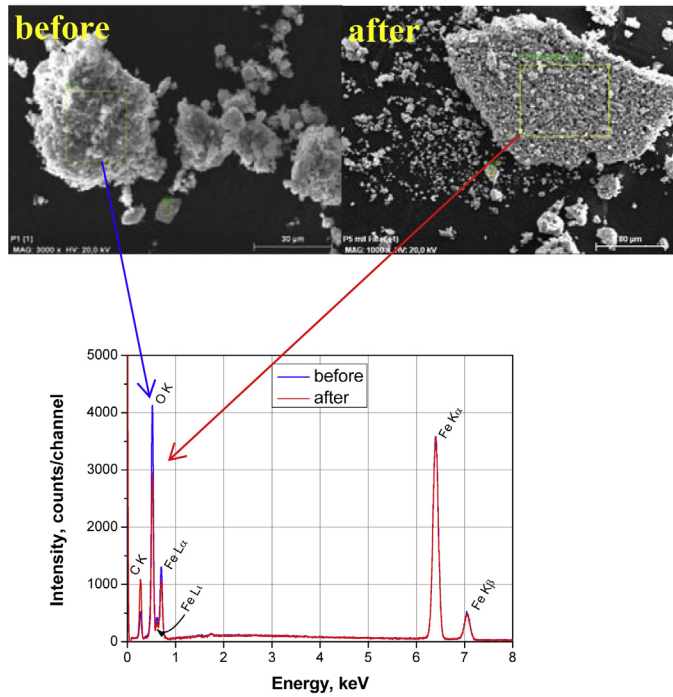


Fig. 10. 20 kV SEM/EDX spectra of FF2 catalyst (normalized in the Fe K α line intensity) before and after the catalytical treatment.

spectra of the FF2 sample before and respectively after the catalytic experiments are shown in Fig. 10.

According to EDX spectra in Fig. 10, no significant change can be observed in the intensity ratio between the two low energy lines O K and Fe K α . Note that the lower intensities of both O K and Fe K α in the "after" EDX spectrum are due to different absorptions related to different morphologies of the analyzed samples. The carbon signal in the EDX spectrum of the sample after treatment is significantly higher. This does not necessarily mean that there is more carbon in the respective sample. It should be kept in mind that the

samples were fixed on SEM sample holders by means of usual carbon tabs, which may contribute more or less to the C K signal from the sample.

In our study 10,11-epoxy-CBZ, 10,11-dihydrocarbamazepine and 2-hydroxy-CBZ have been detected as principal oxidation products by a scan mode screening with HPLC-MS-MS (Fig. S1). Similar intermediates were reported by other authors [28]. The oxidation products can be directly attributed to the attack of •OH resulting in the hydroxylation of either the double bond or the aromatic rings of CBZ (+ m/z 16), a major pathway for •OH-induced degradation of organic molecules. Additionally, an alternative pathway is the attack of •OH on the central seven-membered ring of CBZ, through a non-detected intermediate, to form 10,11-epoxy-CBZ [28][28b]. The intermediates at m/z = 250 were the secondary predominant degradation products. The mechanism might involve an intramolecular reaction, with H₂O loss arising from a non-detected transient dihydroxy-CBZ radical and/or quinoid-CBZ. Similar intermediates were detected in the photodegradation of CBZ with Fe³⁺ [29], photocatalytic degradation of CBZ by TiO₂ [28][28b], and CBZ degradation by ultrasonic/Fe⁰/H₂O₂ [28][28c]. As proposed for other phenolic compounds, we assumed that the degradation mechanism in the presence of H₂O₂ involved •OH radical attack. Furthermore, an oxidative ring-cleavage by hydroxyl radical attack leads to aliphatic compound formation, such as HCOOH, CH₃COOH, and CH₃CHO, and finally, to CO₂ [4].

4. Conclusions

In this study five iron oxalate core–shell magnetite nanoparticles catalysts were evaluated as magnetic heterogeneous Fenton catalysts. The samples are agglomerated with agglomerates sizes over a large range of several μ m up to more than 100 μ m. The individual nanoparticles of rather spherical-like shape have a size between 10 and 20 nm, coated with roughly the same ultrathin iron oxalate shell of 1–2 nm, was confirmed by high resolution transmission electron microscopy (HRTEM) and scanning electron microscopy (SEM). Furthermore, the cores were constituted of crystalline material and the shells were amorphous in nature. The

catalysts exhibited a superparamagnetic behavior. The EDX spectra and XRD patterns of coated catalysts were typical for pure magnetite. The observed FTIR peaks confirm the complexation of the iron oxalate by magnetite surface. The highest degradation rates were observed for two catalysts with largest iron oxalate shell thickness. The optimum experimental parameters were found to be 1.0 g L^{-1} of FF2 or FF3 catalysts, $10\text{ mM H}_2\text{O}_2$, under UV irradiation. More than 99% of both micropollutants were removed after 30 min of reaction time under the above experimental conditions. The results obtained show that the synthesized catalysts are suitable candidates for the removal of pollutants in wastewaters by means of the Fenton heterogeneous reaction.

Acknowledgements

The authors acknowledge the financial support of the Romanian Ministry of National Education CNCS-UEFISCDI through the national grant type PN-II-ID-PCE-2012-4-0477 and BAM Institute; the authors also thank to Dr. V. Nica (XRD analyses), Dr. P. Postolache (VSM measurements) and Prof. Dr. A. Pui (FTIR recordings) from 'Alexandru Ioan Cuza' University in Iasi.

Appendix A. Supplementary data

Supplementary data associated with this article can be found, in the online version, at <http://dx.doi.org/10.1016/j.apcatb.2015.04.050>.

References

- [1] (a) E.J. Routledge, D. Sheahan, C. Desbrow, G.C. Brighty, M. Waldock, J.P. Sumpter, *Environ. Sci. Technol.* 32 (1998) 1559–1565; (b) E.J. Routledge, J.P. Sumpter, *Environ. Toxicol. Chem.* 15 (3) (1996) 241–248; (c) J. Jahnel, M. Neamtu, D. Schudoma, F.H. Frimmel, *Acta Hydrochim. Hydrobiol.* 34 (4) (2006) 389–397.
- [2] A. Krishnan, P. Stathis, S. Permuth, L. Tokes, D. Feldman, *Endocrinology* 132 (6) (1993) 2279–2286.
- [3] M. Clara, B. Strenn, N. Kreuzinger, *Water Res.* 38 (4) (2004) 947–954.
- [4] M. Neamtu, D. Grandjean, A. Sienkiewicz, S. Le Faucheur, V. Slaveykova, J. Velez Colmenares, C. Pulgarín, F.L. De Alencastro, *Appl. Catal. B* 158–159 (2014) 30–37.
- [5] Y.I. Matatov-Meytal, M. Sheintuch, *Ind. Eng. Chem. Res.* 37 (1998) 309–326.
- [6] (a) C. Nadejde, M. Neamtu, R.J. Schneider, V.-D. Hodoroaba, G. Ababei, U. Panne, *Appl. Surf. Sci.* (2015), <http://dx.doi.org/10.1016/j.apsusc.2015.01.036>, in press; (b) Z.H. Ai, Z.H. Gao, L. Zhang, W. He, J.J. Yin, *Environ. Sci. Technol.* 47 (2013) 5344–5352; (c) N. Ferroudj, J. Nzimato, A. Davidson, D. Talbot, E. Briot, V. Dupuis, A. Bee, M. Salah Medjram, S. Abramson, *Appl. Catal. B* 136–137 (2013) 9–18; (d) R.C.C. Costa, M. De Fatima, F. Lelis, L.C.A. Oliveira, J.D. Fabris, J.D. Ardisson, R.R.V.A. Rios, C.N. Silva, R.M. Lago, *Catal. Commun.* 4 (2003) 525–529; (e) R. Matta, K. Hanna, S. Chiron, *Sci. Total. Environ.* 385 (1–3) (2007) 242–251; (f) L. Xu, J. Wang, J. Harzard, *Mater.* 186 (2011) 256–264; (g) X. Xue, K. Hanna, C.H. Despas, F. Wu, N. Deng, *J. Mol. Catal. A* 311 (2009) 29–35; (h) S.-P. Sun, A.T. Lemley, *J. Mol. Catal. A Chem.* 349 (2011) 71–79;
- [7] (i) T. Shahwan, S. Abu Sirriah, M. Nairat, E. Boyaci, A.E. Eroglu, T.B. Scott, K.R. Hallam, *Chem. Eng. J.* 172 (2011) 258–266; (j) S. Shin, H. Yoon, J. Jang, *Catal. Commun.* 10 (2008) 178–182; (k) G. Zelmatov, R. Semiat, *Water Res.* 42 (2008) 492–498.
- [8] (a) H. Tong, S. Ouyang, Y. Bi, N. Umezawa, M. Oshikiri, J. Ye, *Adv. Mater.* 24 (2012) 229–251; (b) M. Xia, C. Chen, M. Long, C. Chen, W. Cai, B. Zhou, *Micropor. Mesopor. Mater.* 145 (2011) 217–223; (c) T.D. Nguyen, N.H. Phan, M.H. Phan, M.H. Do, K.T.J. Ngo, *J. Hazard. Mater.* 185 (2011) 653–661; (d) U. Jeong, X. Teng, Y. Wang, H. Yang, Y. Xia, *Adv. Mater.* 19 (1) (2007) 33–60; (e) T. Valdes-Solis, P. Valle-Vignon, M. Sevilla, A.B. Fuertes, *J. Catal.* 251 (2007) 239–243; (f) T. Valdes-Solis, P. Valle-Vignon, S. Alvares, G. Marban, A.B. Fuertes, *Catal. Commun.* 8 (2007) 2037–2042.
- [9] (g) M.A. Voinov, J.O. Sosa, S. Pagan, E. Morrison, T.I. Smirnova, A.I. Smirnov, *J. Am. Chem. Soc.* 133 (2011) 35–41.
- [10] (h) L. Wang, K.G. Neoh, E.T. Kang, B. Shuter, S.C. Wang, *Adv. Funct. Mater.* 19 (2009) 2615–2622; (i) N. Lewinski, V. Colvin, R. Drezek, *Small* 4 (2008) 26–49; (j) M. Auffan, W. Achouak, J. Rose, M.A. Roncato, C. Chaneac, D.T. Waite, A. Masion, J.C. Woicik, M.R. Wiesner, J.Y. Bottero, *Environ. Sci. Technol.* 42 (2008) 6730–6735.
- [11] (k) W. Cheng, K. Tang, Y. Qi, J. Sheng, Z. Liu, *J. Mater. Chem.* 20 (2010) 1799–1805.
- [12] (l) (a) Y.J. Xiong, J.M. McLellan, Y.D. Yin, Y.N. Xia, *Angew. Chem. Int. Ed.* 46 (5) (2007) 790–794; (b) M.P. Mallin, C.J. Murphy, *Nano Lett.* 2 (2002) 1235–1237; (c) K.R. Brown, D.G. Walter, M.J. Natan, *Chem. Mater.* 12 (2000) 306–313.
- [13] (d) L. Signorini, L. Pasquini, L. Savini, R. Carboni, F. Boscherini, E. Bonetti, A. Giglia, M. Pedio, N. Mahne, S. Nannarone, *Phys. Rev. B* 68 (2003), 195423–1–8.
- [14] (e) L.T. Kuhn, A. Bojesen, L. Timmermann, M.M. Nielsen, S. Mørup, *J. Phys. Condens. Matter* 14 (2002) 13551–13567.
- [15] (f) A. Defoin, R. Defoin-Straatmann, K. Hildenbrand, E. Bittersmann, D. Kreft, H.J. Kühn, *J. Photochem.* 33 (1986) 237–255.
- [16] (g) B. Tanhaei, A. Ayati, M. Lahtinen, M. Sillanpää, *Chem. Eng. J.* 259 (2015) 1–10.
- [17] (h) (a) B.D. Cullity, *Elements of X-ray Diffraction*, third ed., Addison-Wesley, Reading, MA, 1967; (b) M.S. Batista, M.A. Morales, E. Baggio-Saitovich, E.A. Urquieta-Gonzalez, *Hyperfine Interact.* 134 (2001) 161–166.
- [18] (c) S. Peng, C. Wang, J. Xie, S. Sun, *J. Am. Chem. Soc.* 128 (2006) 10676–10677; (d) M.C. Mascolo, Y. Pei, T.A. Ring, *Materials* 6 (2013) 5549–5567.
- [19] (e) L.P. Zhu, H.M. Xiao, W.D. Zhang, G. Yang, S.Y. Fu, *Cryst. Growth Des.* 8 (2008) 963–975.
- [20] (f) Y. Lion, M. Delmelle, A. Van der Vorst, *Nature* 263 (1976) 442–443.
- [21] (g) Y. Nosaka, H. Natsui, M. Sasagawa, A.Y. Nosaka, *J. Phys. Chem. B* 110 (2006) 12993–12999.
- [22] (h) T. Ando, T. Yoshikawa, T. Tanigawa, M. Kohno, N. Yoshida, M. Kondo, *Life Sci.* 61 (1997) 1953–1959.
- [23] (i) C. Gorski, R.M. Handler, B.L. Beard, T. Pasararnis, C.M. Johnson, M.M. Scherer, *Environ. Sci. Technol.* 46 (2012) 12399–12407.
- [24] (j) (a) N. Guo, Y. Liang, S. Lan, L. Liu, J. Zhang, G. Ji, S. Gan, *J. Phys. Chem. C* 118 (2014) 18343–18355; (b) X.W. Cheng, X.J. Yua, Z.P. Xing, *Appl. Surf. Sci.* 258 (2012) 3244–3248.
- [25] (k) E. Brillas, I. Sireis, M.A. Oturan, *Chem. Rev.* 109 (2009) 6570–6631.
- [26] (l) G. Centi, S. Perathoner, T. Torre, M.G. Verduna, *Catal. Today* 55 (2000) 61–69.
- [27] (m) S.-P. Sun, X. Zeng, C. Li, A.T. Lemley, *Chem. Eng. J.* 244 (2014) 44–49.
- [28] (n) (a) M. Cleuvers, *Toxicol. Lett.* 142 (2003) 185–194; (b) C. Carlsson, A.-K. Johansson, G. Alvan, K. Bergman, T. Kühler, *Sci. Total. Environ.* 364 (2006) 67–68.
- [29] (o) (a) S.-P. Sun, X. Zeng, C. Li, A.T. Lemley, *J. Hazard. Mater.* 252–253 (2013) 155–165; (b) C. Martínez, M.L. Canle, M.I. Fernández, J.A. Santaballa, J. Faria, *Appl. Catal. B* 102 (2011) 563–571; (c) A. Ghauch, H. Baydoun, P. Dermesropian, *Chem. Eng. J.* 172 (2011) 18–27.
- [30] (p) S. Chiron, C. Minero, D. Vione, *Environ. Sci. Technol.* 40 (2006) 5977–5983.